Fused-ring induced end-on orientation in conjugated molecular dyads toward efficient single-component organic solar cells

Item Type	Article
Authors	Xia, Dongdong; Zhou, Shengxi; Tan, Wen Liang; Karuthedath, Safakath; Xiao, Chengyi; Zhao, Chaowei; Laquai, Frédéric; McNeill, Christopher R.; Li, Weiwei
Citation	Xia, D., Zhou, S., Tan, W. L., Karuthedath, S., Xiao, C., Zhao, C., Laquai, F., McNeill, C. R., & Li, W. (2022). Fused-ring induced end-on orientation in conjugated molecular dyads toward efficient single-component organic solar cells. Aggregate. Portico. https://doi.org/10.1002/agt2.279
Eprint version	Publisher's Version/PDF
DOI	10.1002/agt2.279
Publisher	Wiley
Journal	Aggregate
Rights	Archived with thanks to Aggregate under a Creative Commons license, details at: http://creativecommons.org/licenses/by/4.0/
Download date	19/09/2023 12:19:11
Item License	http://creativecommons.org/licenses/by/4.0/
Link to Item	http://hdl.handle.net/10754/683220

Aggregate WILEY

Fused-ring induced end-on orientation in conjugated molecular dyads toward efficient single-component organic solar cells

Dongdong Xia[1] | **Shengxi Zhou**[2] | **Wen Liang Tan**[3] | **Safakath Karuthedath**[4] |
Chengyi Xiao[2] | **Chaowei Zhao**[1] | **Frédéric Laquai**[4] | **Christopher R. McNeill**[3] |
Weiwei Li[2]

[1]Institute of Applied Chemistry, Jiangxi Academy of Sciences, Nanchang, China

[2]Beijing Advanced Innovation Center for Soft Matter Science and Engineering & State Key Laboratory of Organic-Inorganic Composites, Beijing University of Chemical Technology, Beijing, China

[3]Department of Materials Science and Engineering, Monash University, Clayton, Australia

[4]KAUST Solar Center (KSC), Physical Sciences and Engineering Division (PSE), Material Science and Engineering Program (MSE), King Abdullah University of Science and Technology (KAUST), Thuwal, Saudi Arabia

Correspondence
Dongdong Xia and Chaowei Zhao, Institute of Applied Chemistry, Jiangxi Academy of Sciences, Nanchang 330096, China.
Email: xiadongdong@iccas.ac.cn and zhaochaowei@jxas.ac.cn

Weiwei Li, Beijing Advanced Innovation Center for Soft Matter Science and Engineering & State Key Laboratory of Organic-Inorganic Composites, Beijing University of Chemical Technology, Beijing 100029, China.
Email: liweiwei@iccas.ac.cn

Dongdong Xia and Shengxi Zhou contributed equally to this work.

Abstract
The molecular orientations of conjugated materials on the substrate mainly include edge-on, face-on, and end-on. Edge-on and face-on orientations have been widely observed, while end-on orientation has been rarely reported. Since in organic solar cells (OSCs) charge transport is along the vertical direction, end-on orientation with conjugated backbones perpendicular to the substrate is recognized as the ideal microstructure for OSCs. In this work, we for the first time obtained the preferential end-on orientation in a conjugated molecular dyad that contains a conjugated backbone as donor and perylene bisimide side units as acceptor. This was realized by introducing a fused-ring structure to replace linear terthiophenes with conjugated backbones, yielding F-MDPBI and L-MDPBI respectively. Surprisingly, a shifting trend of the molecular orientation from dominating edge-on in L-MDPBI to preferential end-on in F-MDPBI was observed. As a consequence, vertical charge carrier mobilities in F-MDPBI are one order of magnitude higher than those with preferential edge-on orientation, so single-component OSCs based on this molecular dyad as a single photoactive layer provided a power conversion efficiency of 4.89% compared to 1.70% based on L-MDPBI with preferential edge-on orientation.

KEYWORDS
conjugated molecular dyads, crystallinity, edge-on, end-on, single-component organic solar cells

1 | INTRODUCTION

Bulk-heterojunction organic solar cells (BHJOSCs) with electron donors and acceptors in the photoactive layer have made significant progress in the past two decades with power conversion efficiencies (PCEs) of over 18%.[1–10] Microstructures in the physically mixed donor/acceptor play important roles in the charge generation process, such as

crystalline/amorphous phase, interface, and orientation.[11] For example, face-on orientation with π-π stacking direction that is vertical to the substrate is helpful for charge transport via intermolecular interaction compared to edge-on orientation,[12] which is due to the vertical charge transport in OSCs. Since charges have the optimal transport efficiency along conjugated backbones,[13] it has been proposed that conjugated backbones perpendicular to the substrate are the ideal microstructure in OSCs.

This microstructure is called end-on orientation (Figure 1),[14] but has been rarely reported in BHJOSCs. In general, conjugated backbones or alkyl side units have a non-covalent interaction with the substrate, so edge-on and face-on orientation with alkyl units or conjugated backbones attached to the substrate is the widely observed configuration. Tajima et al. reported that, when poly(3-butylthiophene) contained perfluoroalkyl units at the end of the conjugated backbone, the polymer backbones generated end-on orientation possibly due to the hydrophobic perfluoroalkyl units.[14] They then used this polymer as the interfacial layer in BHJ or bilayer OSCs to control the microstructure, but it was not directly used as a photoactive layer.[15,16] There were some

other physical techniques, such as evaporation of fullerene C60 as column structure (~60 nm diameter) to construct a vertical charge transport channel, but the large domain size is apparently detrimental to exciton separation in OSCs.[17] It will be an interesting task to develop photoactive layers with end-on orientation via the chemical structure design and study their behaviors in OSCs.

In this work, we are able to realize this purpose in conjugated molecular dyads. These molecules contain covalently-linked electron donors and acceptors in single molecules so that they can be applied to the photoactive layer for single-component OSCs (SCOSCs).[18–31] They have precise structures, tunable chemical and physical properties, and well-organized nanostructures, which can be used as a model molecule to study the charge generation process in OSCs.[28] Herein, we selected a conjugated backbone that had been widely used in BHJOSCs as a donor[32,33] and perylene bisimide (PBI) side units as acceptors linked with a dode-cyl unit to construct molecular dyads (L-MDPBI). We then made the structural modification on L-MDPBI, in which the conjugated bridge terthiophene on the conjugated backbone was replaced by fused cyclopentadithiophene (F-MDPBI) (Figure 1A). Surprisingly, compared to L-MDPBI with traditional dominating edge-on orientation, F-MDPBI exhibited preferential end-on orientation (Figure 1B) as confirmed by grazing-incidence wide-angle X-ray scattering (GIWAXS). The distinct orientation enabled F-MDPBI to show high charge carrier mobilities and hence a high PCE of 4.89% in SCOSCs, which is among the highest PCEs in molecular dyads-based SCOSCs until now (Figure 1C).[34]

## 2 | RESULTS AND DISCUSSION

2.1 | Synthesis

The synthetic procedures of L-MDPBI and F-MDPBI are shown in Scheme 1, in which only two synthetic steps were performed with a total yield of ~70%. It is worthy to mention that, herein we developed two key precursors **M2** and **M3** that contained both carbaldehyde (—CHO) and organic stannyl units,[35] which can significantly simplify the synthetic complexity when reacting with another key monomer **M1** containing PBI side units. The two molecule dyads show excellent solubility in most organic solvents, such as $CHCl_3$, toluene, and chlorobenzene (CB), and high thermal stability up to 400°C as confirmed by thermogravimetric analysis (Figure S1A). Differential scanning calorimetry measurements show that both L-MDPBI and F-MDPBI have the transition during the heating and cooling process with similar enthalpies, but the temperature for the transition is relatively low for F-MDPBI (Figure S1B), which is possibly due to the length difference between terthiophene and cyclopentadithiophene bridges.[36]

FIGURE 1 (A) The chemical structures and (B) illustration of edge-on and end-on orientation to the substrate based on the molecular dyads L-MDPBI and F-MDPBI. (C) power conversion efficiencies (PCEs) versus FF of single-component organic solar cells (SCOSCs) based on molecular dyads

2.2 | Absorption spectra and energy levels

Molar optical absorption spectra of L-MDPBI and F-MDPBI in $CHCl_3$ solution and thin films are present in Figure 2A,B, in which absorption spectra of the acceptor PBI (Figure S2)
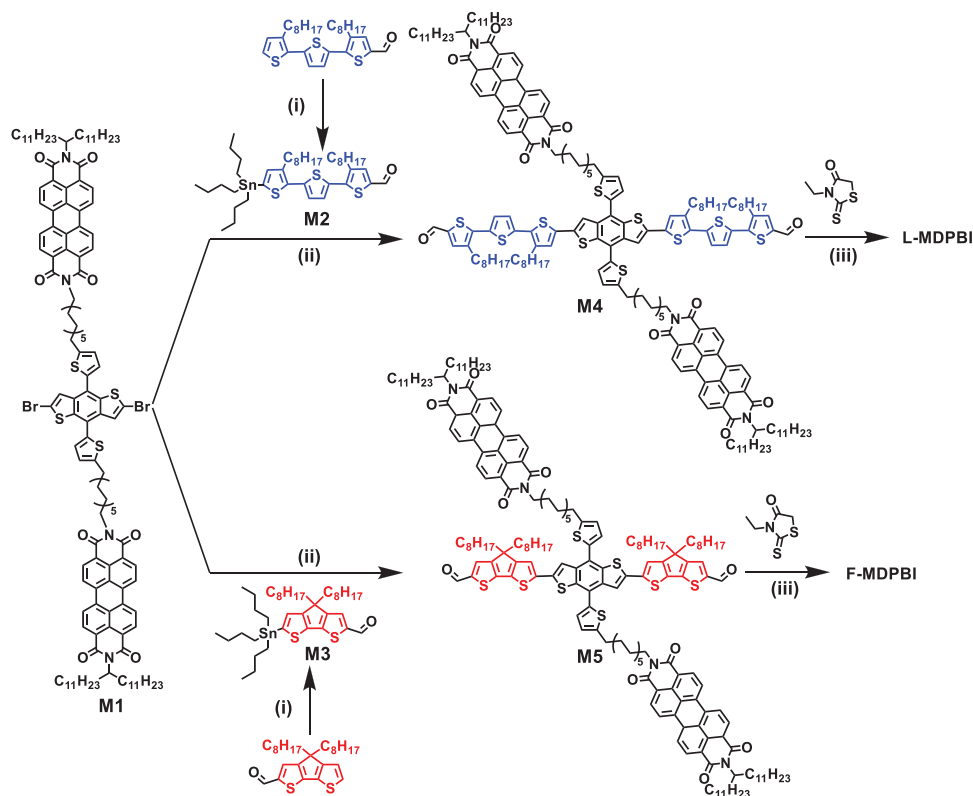
SCHEME 1 Synthetic routes for L-MDPBI and F-MDPBI. (i) tetrahydrofuran (THF), −78°C, N-methylpiperazine, BuLi, tributyltin chloride. (ii) Pd(PPh₃)₄, Toluene, 120°C, 24 h; (iii) CF, piperidine, 80°C, overnight
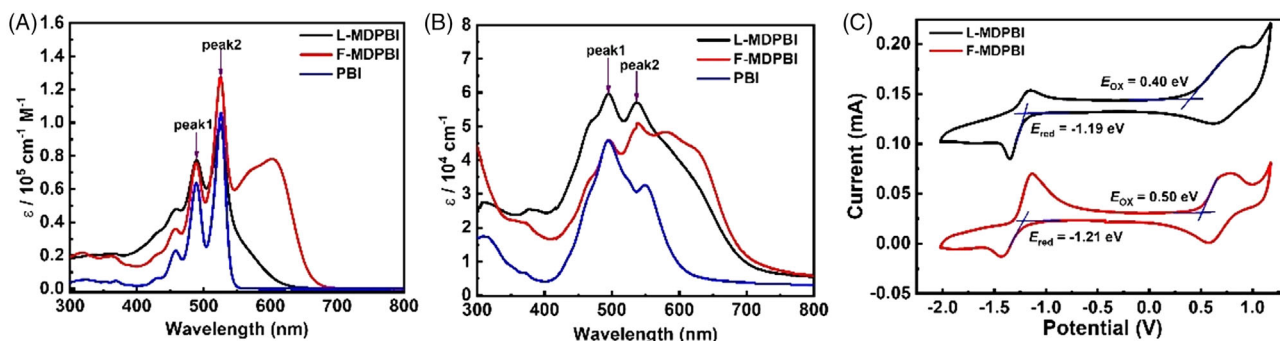

FIGURE 2 Molar optical absorption coefficients of conjugated molecules in (A) CHCl₃ solution and (B) films. The absorption of the molecular perylene bisimide (PBI) is also included. (C) cyclic voltammograms in thin films of L-MDPBI and F-MDPBI. E_{ox} and E_{red} are present in the figure

are also included. Both of them exhibit broad absorption spectra from 400 to 700 nm with the contribution from PBI side units (short wavelength region) and conjugated backbones (long wavelength region). Compared to the absorption in solution, they show red-shift absorption in thin films (∼100 nm), which is consistent with their donor counterparts L-MD and F-MD (Figures S2 and S3).[35] It is noted that F-MDPBI has an absorption band at the long wavelength region (∼620 nm) of its donor backbone in solution, while this band is absent in its donor counterpart F-MD. This indicates that PBI side units can help F-MDPBI to form a pre-aggregate structure in solution, which can be verified by temperature-dependent absorption spectra, as shown in Figure S4. When the temperature was elevated from 30 to 70°C, the intensity of two peaks in the range of 550–600 nm was reduced. In thin films, the peak at ∼490 nm (peak1) can be observed in the two molecular dyads and PBI, and the enhanced intensity of peak 1 related to peak 2 compared to that of the solu-

tion, corresponding to the PBI unit, should be attributed to the H-aggregation of PBIs.[37–44] We further investigated the temperature-dependent photoluminescence spectra, as shown in Figure S4. Consequently, a slight blue shift and intensity decrement can be observed when enhancing the temperature for both L-MDPBI and F-MDPBI solutions.

The frontier energy levels of the molecules were determined by cyclic voltammograms as shown in Figure 2C, in which the highest occupied molecular orbital (HOMO) and lowest unoccupied molecular orbital (LUMO) levels could be calculated from oxidation potential (E_{ox}) and reduction potential (E_{red}). L-MDPBI and F-MDPBI have similar LUMO levels (−3.61 and −3.59 eV) that are determined by PBI side units, while F-MDPBI has a slightly deep HOMO level of −5.30 eV compared to −5.20 eV in L-MDPBI. This illustrates that fused-ring design is able to lower the HOMO level of the molecule, which is helpful to enhance open-circuit voltage (V_{oc}) in solar cells.
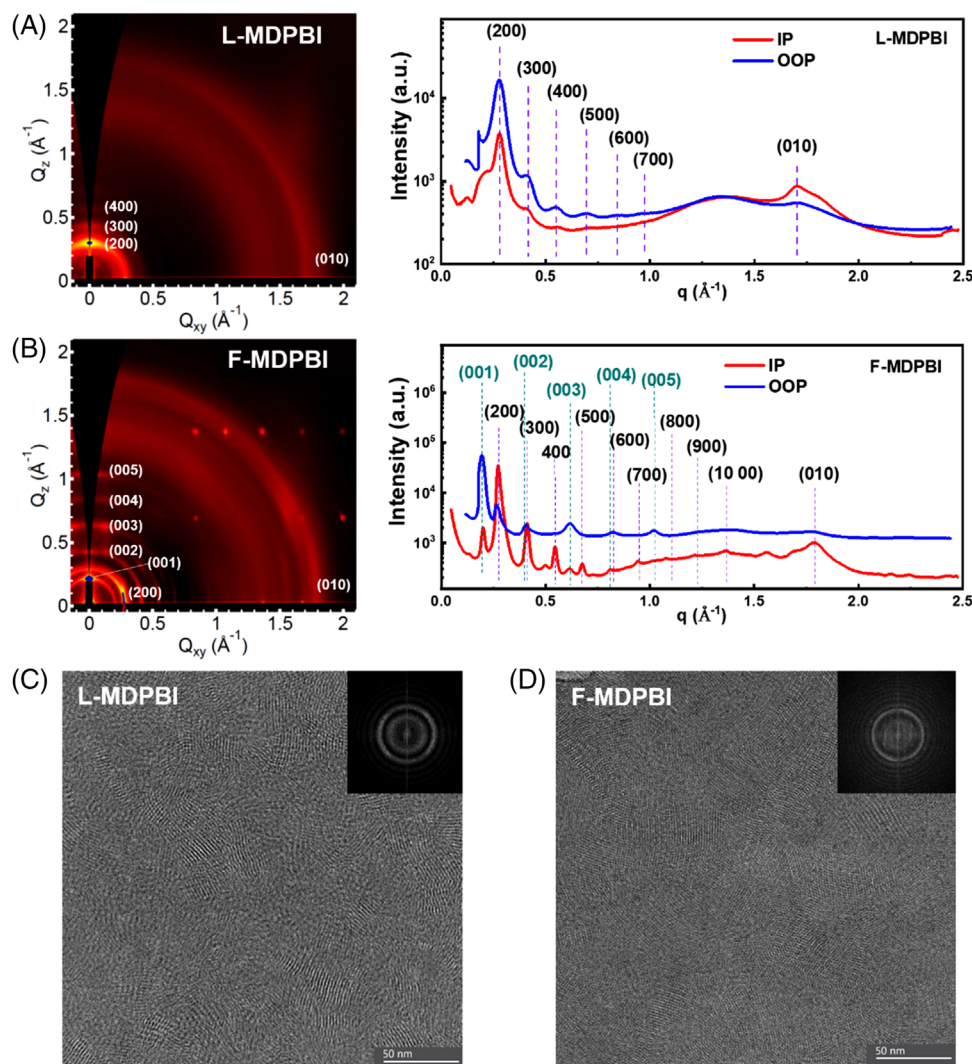
FIGURE 3 GIWAXS images along with the corresponding profiles in thin films on bare Si substrate of (A) L-MDPBI and (B) F-MDPBI. Cryo-transmission electron microscopy (TEM) images of thin films based on (C) L-MDPBI and (D) F-MDPBI (scale bar: 50 nm). Representative Fast Fourier Transforms (FFTs) of the images were also included. L-MDPBI thin films were solution-processed from chlorobenzene (CB) without thermal treatment, and F-MDPBI thin films were solution-processed from CF/1% *o*-DCB/0.5% DIO with thermal treatment at 150°C for 10 min, and then solvent annealing by using tetrahydrofuran (THF) for 30 s. Both are the optimal condition for single-component organic solar cell (SCOSC) devices

2.3 | Crystallinity and molecular orientation

We then studied the crystalline properties of L-MDPBI and F-MDPBI in thin films by GIWAXS measurements, and the results corresponding to the optimized conditions are shown in Figure 3. L-MDPBI, processed by CB, exhibits highly ordered diffraction peaks (*h*00) up to (700) in the out-of-plane (OOP) direction (Figure 3A). The (100) peak was not observed due to the low *q* value beyond the measurement limit. The (200) peak with $q = 0.28$ Å^{-1} is corresponding to a *d*-spacing of 4.50 nm (Table S1), which should be attributed to the lamellar stacking of conjugated backbones. The *d*-spacing here is much less than those in PBI-based double-cable conjugated polymers with *d*-spacings > 6.0 nm.[38] This indicates that PBIs in L-MDPBI have excellent *H*-aggregation so as to provide reduced *d*-spacing (Figure 1B). It should be noted that this *d*-spacing is not attributed to the length of the conjugated backbone, which should be a length of ~3.66 nm that was calculated from the optimized geometry via the density functional theory method (Figure S5A). The (010) peak in the in-plane (IP) direction with $q =$

1.70 Å^{-1} ($d = 3.70$ Å) is attributed to π-π stacking of conjugated backbones and PBI side units. From the analysis above, we can conclude that L-MDPBI has a preferential edge-on orientation to the substrate as depicted in Figure 1B.

For comparison, GIWAXS of F-MDPBI films processed by pure CB or CHCl$_3$ was also measured. As a result, there are no obvious diffraction peaks observed indicating an amorphous state of F-MDPBI (Figures S6–S8). However, F-MDPBI, processed by chloroform with *o*-dichlorobenzene (*o*-DCB) and 1,8-diiodooctane (DIO) as co-additives, exhibits completely different diffraction peaks in GIWAXS measurement, which can be further improved by thermal or solvent annealing (Figure 3B and Figure S8). This can also be reflected by their absorption spectra in thin films, in which the thin film thermal-treated at 150°C exhibited enhanced intensity (Figure S9).

We then analyze the diffraction peaks of F-MDPBI thin films fabricated from CF/1% *o*-DCB/0.5% DIO with thermal treatment at 150°C for 10 min and then solvent annealing by using tetrahydrofuran for 30 s (Figure 3). The highly ordered diffraction peaks (*h*00) up to (10 00) are observed in the

TABLE 1 Photovoltaic parameters of single-component organic solar cells (SCOSCs) and hole mobilities exacted from organic field-effect transistor (OFET) devices (μ_h^H) and space-charge limit current (SCLC) measurement (μ_h^V)[a]

	J_{sc} (mA/cm²)	V_{oc} (V)	FF	PCE (%)	μ_h^H (cm² V⁻¹ s⁻¹)	μ_h^V (cm² V⁻¹ s⁻¹)
L-MDPBI	5.46 (5.36 ± 0.08)	0.82 (0.805 ± 0.007)	0.38 (0.38 ± 0.01)	1.70 (1.65 ± 0.04)	6.21×10^{-5}	6.0×10^{-4}
F-MDPBI	9.44 (9.58 ± 0.16)	0.87 (0.879 ± 0.009)	0.59 (0.56 ± 0.02)	4.89 (4.78 ± 0.05)	4.88×10^{-5}	4.9×10^{-3}

[a]Statistics in parentheses from 6 independent cells.

IP direction, exhibiting a similar d-spacing of 4.57 nm with L-MDPBI (Table S2). Meanwhile, in the OOP direction, a new set of diffraction peaks are present with a d-spacing of 3.17 nm, which is slightly less than the length of conjugated backbones (3.47 nm, Figure S5B). Therefore, these peaks are assigned as (00h) peaks up to (005). The (010) peak with $q = 1.79$ Å⁻¹ ($d = 3.51$ Å) is only observed in the IP direction but is absent in the OOP direction. All these signals confirm the preferential end-on orientation in F-MDPBI thin film as shown in Figure 1B, in which the conjugated backbones are perpendicular to the substrate.

Moreover, we tried to optimize the L-MDPBI film under identical conditions to F-MDPBI for ideal end-on orientation, but L-MDPBI still present dominating edge-on orientation (Figure S7). It should also be noted that F-MDPBI has better crystallinity according to the strong and sharp peaks in GIWAXS images, and also exhibits close π-π stacking of conjugated backbones (or PBI units) from the small d-spacing of (010) peak compared to L-MDPBI. The preferential end-on orientation as well as the strong crystallinity and close packing of conjugated moieties will definitely improve the vertical charge transport in OSCs.

We further used cryo-transmission electron microscopy to study the morphology of molecular dyads, as shown in Figure 3C,D. Both L-MDPBI and F-MDPBI show crystalline fringes with clear peaks observed in the Fast Fourier Transform. The d-spacings were then extracted from the images, in which the (h00) peaks could be observed (Figure S10). This is consistent with GIWAXS measurement. In addition, F-MDPBI shows several halo rings with sharp peaks, indicating its better crystallinity in thin films.
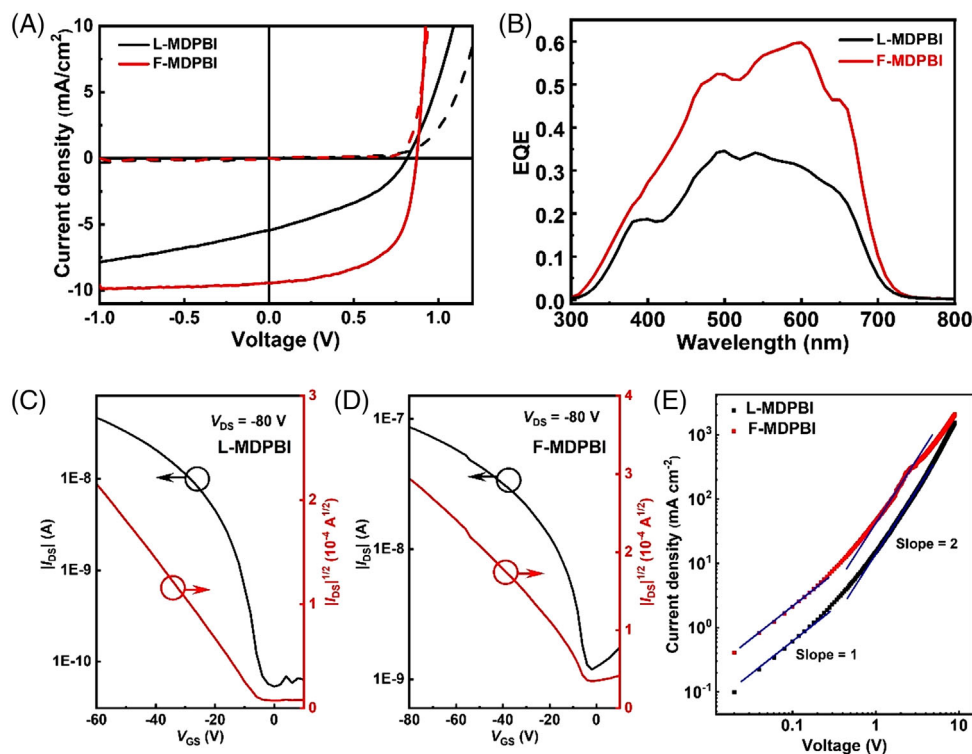
2.4 | Single-component organic solar cells

L-MDPBI and F-MDPBI were then used as photoactive layers to construct SCOSCs with an inverted configuration of ITO/ZnO/MDPBI/MoO₃/Ag. The fabrication conditions, including solvents, additives, thermal annealing, and solvent annealing, were systematically attempted for the photoactive layers in order to obtain the optimized performance (Tables S3–S15). In general, both L-MDPBI and F-MDPBI-based SCOSCs were very sensitive to the fabrication conditions. Since L-MDPBI always forms preferential edge-on orientation by casting from different solvents, we attempted several solvents including CB and CHCl₃ without or with additives, in combination with thermal annealing, for L-MDPBI-based SCOSCs (Tables S3 and S5–S9). However, L-MDPBI-based SCOSCs can just provide a moderate PCE of 1.7% after the optimization (Figure 4A and Table 1). For comparison, F-MDPBI thin films fabricated from CB encountered the issue of leakage current in SCOSCs. Nonetheless, F-MDPBI

thin films fabricated from CHCl₃ with o-DCB or DIO as an additive could provide PCEs over 4% in SCOSCs. The best PCE based on F-MDPBI thin film after solvent vapor annealing (SVA) was 4.89% with a high short-circuit current density (J_{sc}) of 9.44 mA/cm², a V_{oc} of 0.87 V, and fill factor (FF) of 0.59, which are significantly higher than those based on L-MDPBI (Figure 4A and Table 1). The FF is also among the highest values in SCOSCs based on molecular dyads (Figure 1C, Figure S11, and Table S16), indicating efficient charge generation in F-MDPBI-based solar cells. High J_{sc}s were also reflected by their external quantum efficiencies (EQEs) with broad photoresponse from 300 to 700 nm (Figure 4B), in which F-MDPBI-based SCOSCs had high EQEs up to 0.60, but EQEs for L-MDPBI based solar cells were below 0.35.

2.5 | Charge carrier mobilities based on the organic field-effect transistor and space-charge limit current measurement

We further used organic field-effect transistor (OFET) with a bottom gate–bottom contact (BGBC) configuration and space-charge limit current (SCLC) measurements to probe charge mobilities in the horizontal and vertical direction, respectively. Transfer curves obtained from BGBC OFET devices with these molecular dyad films are shown in Figure 4C,D, and the hole mobility in the horizontal direction (μ_h^H) can be evaluated. As a result, comparable μ_h^H values of 6.21×10^{-5} cm² V s⁻¹ and 4.88×10^{-5} cm² V s⁻¹ are obtained for L-MDPBI and F-MDPBI, respectively (Table 1). While the on/off ratio of L-MDPBI (8.66×10^2) is one order higher than that of F-MDPBI (7.27×10^1). Dark J-V curves of hole-only devices are also shown in Figure 4E, and the average hole mobilities in the vertical direction (μ_h^V) of each molecular dyad were calculated through the SCLC method. As a consequence, the μ_h^V are 6.0×10^{-4} cm² V s⁻¹ for L-MDPBI and 4.9×10^{-3} cm² V s⁻¹ for F-MDPBI, respectively (Table 1). Obviously, the μ_h^V of F-MDPBI with preferential end-on orientation is almost one order of magnitude higher than that of L-MDPBI with dominating edge-on orientation.[45,46] These remarkable differences of μ_h^H and μ_h^V between L-MDPBI with preferential edge-on orientation and F-MDPBI with preferential end-on orientation should be owing to the evolution of their aggregation states, since edge-on and end-on orientations are beneficial for charge transport in the horizontal and vertical directions, respectively, as illustrated in Figure 1B.[47] Furthermore, the electron mobilities in the vertical direction (μ_e^V) were explored by the SCLC method with electron-only devices. The μ_e^V is 4.12×10^{-4} cm² V s⁻¹ for F-MDPBI and 5.87×10^{-5} cm² V s⁻¹ for L-MDPBI (Figure S12). Obviously, both μ_h^V and μ_e^V are

FIGURE 4 (A) *J-V* characteristics under AM 1.5G illumination and (B) the corresponding external quantum efficiency (EQE) curves of optimized single-component organic solar cells (SCOSCs) based on L-MDPBI and F-MDPBI. Transfer curves were obtained from the bottom gate–bottom contact (BGBC) field-effect transistor (FET) devices with molecular dyad thin films (C) L-MDPBI and (D) F-MDPBI. (E) Dark *J-V* curves of hole-only devices with the configuration of ITO/PEDOT:PSS/active layer/MoO$_3$/Ag
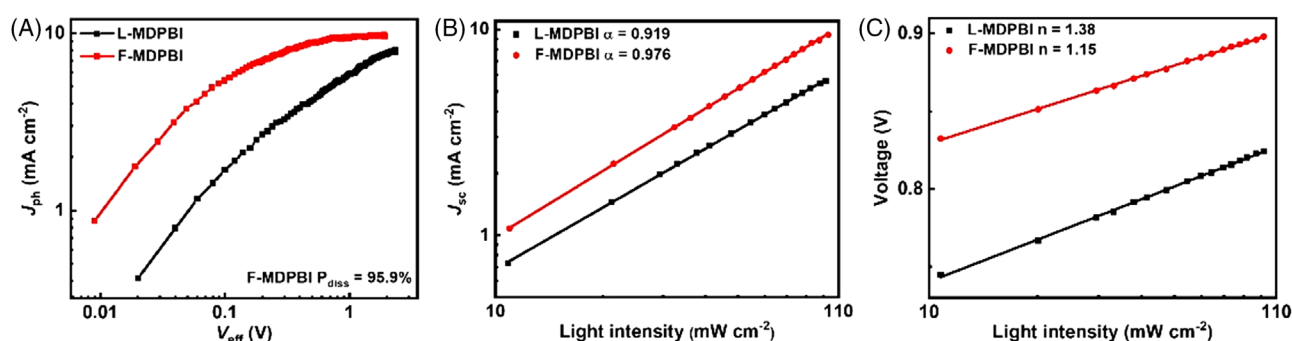
FIGURE 5 Characterization of exciton dissociation, charge generation, and recombination processes of devices based on L-MDPBI and F-MDPBI. (A) J_{ph}−V_{eff} curves, (B) J_{sc}−light intensity fitting lines, and (C) V_{oc}−light intensity fitting lines

significantly higher in F-MDPBI film, which is helpful for facilitating exciton dissociation and charge transport.

2.6 | Charge dissociation, extraction, and recombination

To evaluate the efficiency of charge generation and extraction, the relation of photocurrent density (J_{ph}) versus effective voltage (V_{eff}) of OSCs based on molecular dyads is analyzed, and the curves are shown in Figure 5A. J_{ph} is defined as J_{light} − J_{dark}, where J_{light} and J_{dark} are obtained from current densities under light illumination at AM1.5G and dark conditions, respectively. V_{eff} is equal to $V_0 − V_a$, where V_0 is the voltage at which $J_{ph} = 0$ and V_a is the applied bias voltage. The charge collection probability (P(E, T))[48] is elucidated as J_{ph}/J_{sat},

where J_{sat} is a saturation of J_{ph} value at $V_{eff} \geq 2$ V. In general, high P(E, T) corresponds to a more efficient exciton dissociation and charge collection processes. When the efficient voltage is 2 V, the J_{ph} of L-MDPBI does not reach a saturation value, but the J_{ph} of F-MDPBI is at the saturation value, according to the J_{ph} and J_{sc}, the P(E, T) can be calculated as 95.9%. Therefore, F-MDPBI with preferential end-on orientation can provide more exciton dissociation and efficient charge transport to the electrodes, resulting in improved J_{sc}s in the devices.

We also examined the charge recombination through the variation of J_{sc} and V_{oc} as a function of the incident light intensity (P_{Light}) of L-MDPBI and F-MDPBI. The dependence of J_{sc} and P_{Light} is plotted in Figure 5B. The relationship between J_{sc} and P_{Light} is related to the equation[49]: $J_{sc} \propto P_{Light}{}^\alpha$, where α is the exponential factor, whose value
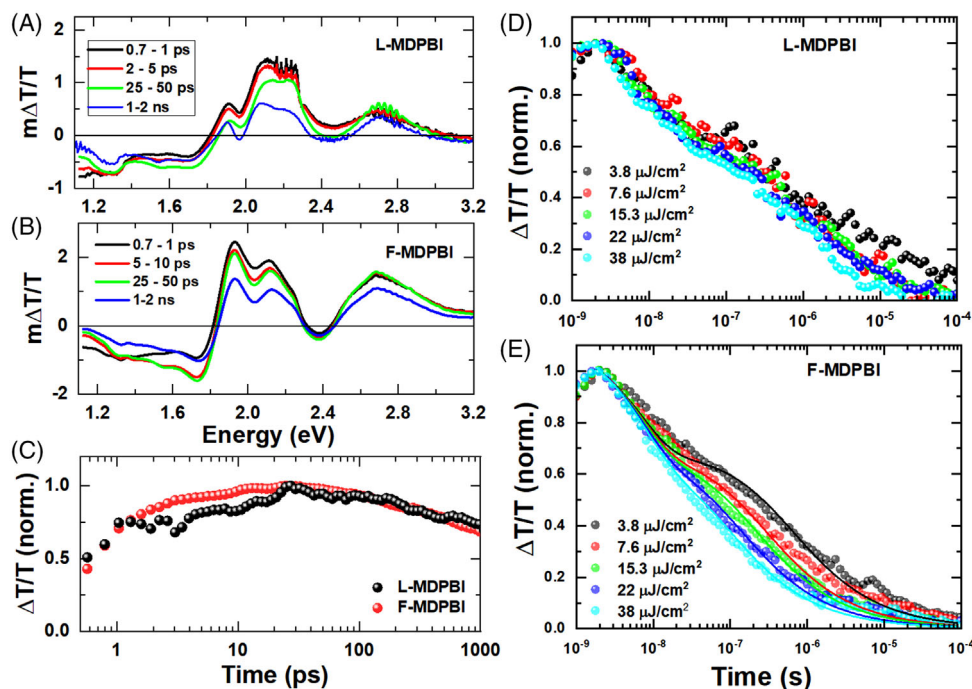
FIGURE 6 Picosecond-nanoseocnd TA spectra of (A) L-MDPBI and (B) F-MDPBI. (C) Normalized kinetics of 1.7 eV region of L-MDPBI (black symbols) and F-MDPBI (red symbols). Nanosecond-microsecond transient absorption (TA) kinetics of 1.6–1.7 eV region for a range of fluences of (D) L-MDPBI and (E) F-MDPBI. The solid line in (E) shows the global fit

can be obtained from the slopes of fitting lines. Herein, the α value was calculated to be 0.919 for L-MDPBI. While in the device based on F-MDPBI, the α value was estimated to be 0.976, which is closer to 1 compared with L-MDPBI, indicating negligible second-order recombination in the F-MDPBI-based OSCs. Meanwhile, Figure 5C shows the V_{oc} curves of molecular dyads-based devices under different P_{Light} varying from 10 to 100 mW cm^{-2}. In general, the slope of the fitting line will be close to 2 kBT/q when monomolecular recombination dominates in the devices, but if bimolecular recombination dominates, the slope will be close to 1 kBT/q.[50] From the V_{oc}–P_{Light} plots, the slope was calculated to be 1.38 for L-MDPBI and 1.15 for F-MDPBI, respectively. This implies that monomolecular recombination in F-MDPBI is less than that in L-MDPBI, which is in favor of achieving higher FF and device performance compared to L-MDPBI.

2.7 | Ultrafast transient absorption spectroscopy

To investigate the excited state dynamics in these solar cells, we performed ultrafast transient absorption (TA) spectroscopy measurements on thin films of the active layer. Figure 6A,B shows the picosecond-nanosecond TA spectra of the L- and F-MDPBI film excited with 600 nm laser pulses. The positive $\Delta T/T$ signal represents the ground state bleach, and the negative $\Delta T/T$ shows the photo-induced absorption (PIA) region.[51] In Figure 6B, two PIA bands were observed immediately after excitation, respectively at 1.3 eV and 1.7 eV (black line). The 1.3 eV band started to decay while the 1.6–1.7 eV one kept growing till 50 ps, indicating the charge generation (Figure 6C). The charge

generation kinetics in F-MDPBI films (Figure 6C, red symbols) show a clear ultrafast and diffusion-mediated charge generation. Although the TA spectra of L-MDPBI showed a very different shape than F-MDPBI, the kinetics evolution is comparable (Figure 6C, black symbols). In both cases, the excitation at 600 nm generated charge carriers (charge transfer state/CT state) effectively; hence the performance difference should come from CT state separation to free charge formation.

Figure 6D and e show the ns-μs TA kinetics of the 1.6–1.7 eV band of both films excited at 532 nm for a wide range of fluences as noted in the legend. Corresponding TA spectra can be found in the supporting information (Figure S13). The charge carriers showed a fluence-independent decay initially and then showed dependence at a later stage of F-MDPBI films. This fluence independence is a typical signature of the geminate recombination of CT states and non-geminate recombination of free charge carriers (fluence dependency). The kinetics of the same spectral region for L-MDPBI showed very clear fluence independence for the range fluences we measured (Figure 6D). We performed a global fit to quantify the non-geminate recombination rate (β) of free charge carriers and the free charge carrier yield of F-MDPBI (the solid lines in Figure 6E).[52,53] We obtained a β of 9×10^{-13} cm^3/s and a 68 % of free charge carriers from the fit. A similar analysis was not possible for L-MDPBI as the decay shows almost no fluence dependency. This indicates that most of the CT states in L-MDPBI are recombined to decay to the ground state without forming enough free charges to generate photocurrent. Thus, from the TA spectroscopy, we can conclude that F-MDPBI and L-MDPBI possess similar charge generation kinetics and yield the same CT state, but the separation of CT state to free charges is different. This difference can be attributed to the molecular

orientation in film morphology. The vertical delocalization of holes in an F-MDPBI-based device with preferential end-on orientation is expected to have a larger effective distance and weaker coulombic interaction in CT state separation than those in the L-MDPBI-based device with preferential edge-on orientation.[16] This can effectively facilitate CT state separation into free charges and enhance the vertical hole mobility to promote free charge transport to the electrode simultaneously. All of these can contribute to less non-geminate recombination and generate more free charges, which is consistent with the results of SCLC and single-component solar cell performance.

An interesting question is why fused-ring structures can switch the molecular orientation from dominating edge-on to preferential end-on. We studied the crystalline structures of the donor molecules L-MD and F-MD by GIWAXS measurement and found that both of them exhibited preferential edge-on orientation (Figure S14 and Tables S17–S18). This reveals that the introduction of PBI side units causes the preferential end-on orientation of F-MDPBI. Contact angle measurements via water and glycol on the thin films were then performed (Figure S15 and Table S19). According to the data of surface energy and Flory–Huggins interaction parameter (χ), F-MDPBI shows a lower χ value, implying better miscibility with the ZnO layer compared to L-MDPBI, but this is still difficult to explain the preferential end-on orientation. From the GIWAXS analysis above, it seems that the co-additive of *o*-DCB/DIO is the key factor to induce preferential end-on orientation of F-MDPBI, but the reason behind this is unclear.

3 | CONCLUSION

In conclusion, we have developed two conjugated molecular dyads containing conjugated backbones as electron donors and PBI side units as acceptors. When using fused conjugated bridges to replace linear bridges, the molecular orientation on the substrate shifted from dominating edge-on to preferential end-on, which facilitates vertical charge transport in OSCs. As a result, F-MDPBI with preferential end-on orientation was used as a single photoactive layer in SCOSCs, providing a PCE of 4.89% with an outstanding FF of 0.59. This is the first example to realize preferential end-on orientation in OSCs, and the results demonstrate that fused-ring design is a powerful strategy in developing new molecular dyads for high-performance SCOSCs.

AUTHOR CONTRIBUTIONS
Dongdong Xia and Shengxi Zhou contributed equally to this work; Dongdong Xia synthesized the materials, characterized the solar cells, and carried out the detailed characterization; Shengxi Zhou characterized the solar cells and contact angle measurement; Wen Liang Tan and Christopher R. McNeill performed the GIMAXS measurement and data analysis; Safakath Karuthedath and Frédéric Laquai carried out the TA measurement and data analysis; Chengyi Xiao performed OFETs measurement; Dongdong Xia, Chaowei Zhao, and Weiwei Li prepared the manuscript; Weiwei Li supervised and directed this project. All authors discussed the results and commented on the manuscript.

CONFLICT OF INTEREST
The authors declare no conflict of interest.

ORCID
Dongdong Xia https://orcid.org/0000-0002-4520-0992

REFERENCES
1. J. Xiong, J. Xu, Y. Jiang, Z. Xiao, Q. Bao, F. Hao, Y. Feng, B. Zhang, Z. Jin, L. Ding, *Sci. Bull.* **2020**, *65*, 1792.
2. F. Liu, L. Zhou, W. Liu, Z. Zhou, Q. Yue, W. Zheng, R. Sun, W. Liu, S. Xu, H. Fan, L. Feng, Y. Yi, W. Zhang, X. Zhu, *Adv. Mater.* **2021**, *33*, 2100830.
3. S. Chen, L. Feng, T. Jia, J. Jing, Z. Hu, K. Zhang, F. Huang, *Sci. Chin. Chem.* **2021**, *64*, 1192.
4. C. Li, J. Zhou, J. Song, J. Xu, H. Zhang, X. Zhang, J. Guo, L. Zhu, D. Wei, G. Han, J. Min, Y. Zhang, Z. Xie, Y. Yi, H. Yan, F. Gao, F. Liu, Y. Sun, *Nat. Energy* **2021**, *6*, 605.
5. Y. Liu, B. Liu, C.-Q. Ma, F. Huang, G. Feng, H. Chen, J. Hou, L. Yan, Q. Wei, Q. Luo, Q. Bao, W. Ma, W. Liu, W. Li, X. Wan, X. Hu, Y. Han, Y. Li, Y. Zhou, Y. Zou, Y. Chen, Y. Li, Y. Chen, Z. Tang, Z. Hu, Z.-G. Zhang, Z. Bo, *Sci. Chin. Chem.* **2022**, *65*, 224.
6. Y. Cui, Y. Xu, H. Yao, P. Bi, L. Hong, J. Zhang, Y. Zu, T. Zhang, J. Qin, J. Ren, Z. Chen, C. He, X. Hao, Z. Wei, J. Hou, *Adv. Mater.* **2021**, *33*, 2102420.
7. P. Bi, S. Zhang, Z. Chen, Y. Xu, Y. Cui, T. Zhang, J. Ren, J. Qin, L. Hong, X. Hao, J. Hou, *Joule* **2021**, *5*, 2408.
8. Z. Zheng, J. Wang, P. Bi, J. Ren, Y. Wang, Y. Yang, X. Liu, S. Zhang, J. Hou, *Joule* **2022**, *6*, 171.
9. M. Yang, W. Wei, X. Zhou, Z. Wang, C. Duan, *Energy Mater.* **2021**, *1*, 100008.
10. B. Wu, B. Yin, C. Duan, L. Ding, *J. Semicond.* **2021**, *42*, 080301.
11. Y. Huang, E. J. Kramer, A. J. Heeger, G. C. Bazan, *Chem. Rev.* **2014**, *114*, 7006.
12. C. Piliego, T. W. Holcombe, J. D. Douglas, C. H. Woo, P. M. Beaujuge, J. M. J. Fréchet, *J. Am. Chem. Soc.* **2010**, *132*, 7595.
13. A. Saeki, Y. Koizumi, T. Aida, S. Seki, *Acc. Chem. Res.* **2012**, *45*, 1193.
14. J. Ma, K. Hashimoto, T. Koganezawa, K. Tajima, *J. Am. Chem. Soc.* **2013**, *135*, 9644.
15. F. Wang, K. Hashimoto, H. Segawa, K. Tajima, *ACS Appl. Mater. Interfaces* **2018**, *10*, 8901.
16. F. Wang, K. Nakano, H. Yoshida, K. Hashimoto, H. Segawa, C.-S. Hsu, K. Tajima, *J. Mater. Chem. A* **2018**, *6*, 22889.
17. M. Thomas, W. Li, Z. Bo, M. J. Brett, *Org. Electron.* **2012**, *13*, 2647.
18. S. Liang, X. Jiang, C. Xiao, C. Li, Q. Chen, W. Li, *Acc. Chem. Res.* **2021**, *54*, 2227.
19. Y. He, N. Li, C. J. Brabec, *Org. Mater.* **2021**, *03*, 228.

20. J. Roncali, I. Grosu, *Adv. Sci.* **2019**, *6*, 1801026.

21. W. Wang, R. Sun, J. Guo, J. Guo, J. Min, *Angew. Chem. Int. Ed.* **2019**, *58*, 14556.

22. S. Lucas, J. Kammerer, M. Pfannmöller, R. R. Schröder, Y. He, N. Li, C. J. Brabec, T. Leydecker, P. Samorì, T. Marszalek, W. Pisula, E. Mena-Osteritz, P. Bäuerle, *Sol. RRL* **2021**, *5*, 2000653.

23. S. Lucas, T. Leydecker, P. Samorì, E. Mena-Osteritz, P. Bäuerle, *Chem. Commun.* **2019**, *55*, 14202.

24. A. Bogdan, L. Szolga, G.-I. Giurgi, A. P. Crişan, D. Bogdan, S. Hadsadee, S. Jungsuttiwong, R. Po, I. Grosu, J. Roncali, *Dyes Pigm.* **2021**, *184*, 108845.

25. A. Labrunie, A. H. Habibi, S. Dabos-Seignon, P. Blanchard, C. Cabanetos, *Dyes Pigm.* **2019**, *170*, 107632.

26. T. L. Nguyen, T. H. Lee, B. Gautam, S. Y. Park, K. Gundogdu, J. Y. Kim, H. Y. Woo, *Adv. Funct. Mater.* **2017**, *27*, 1702474.

27. K. Narayanaswamy, A. Venkateswararao, P. Nagarjuna, S. Bishnoi, V. Gupta, S. Chand, S. P. Singh, *Angew. Chem. Int. Ed.* **2016**, *55*, 12334.

28. L. Bu, X. Guo, B. Yu, Y. Qu, Z. Xie, D. Yan, Y. Geng, F. Wang, *J. Am. Chem. Soc.* **2009**, *131*, 13242.

29. J. Roncali, *Adv. Energy Mater.* **2021**, *11*, 2102987.

30. Y. He, T. Heumüller, W. Lai, G. Feng, A. Classen, X. Du, C. Liu, W. Li, N. Li, C. J. Brabec, *Adv. Energy Mater.* **2019**, *9*, 1900409.

31. Y. He, B. Wang, L. Lüer, G. Feng, A. Osvet, T. Heumüller, C. Liu, W. Li, D. M. Guldi, N. Li, C. J. Brabec, *Adv. Energy Mater.* **2022**, *12*, 2103406.

32. Y. Chen, X. Wan, G. Long, *Acc. Chem. Res.* **2013**, *46*, 2645.

33. Q. Zhang, B. Kan, F. Liu, G. Long, X. Wan, X. Chen, Y. Zuo, W. Ni, H. Zhang, M. Li, Z. Hu, F. Huang, Y. Cao, Z. Liang, M. Zhang, T. P. Russell, Y. Chen, *Nat. Photon.* **2015**, *9*, 35.

34. A. Aubele, Y. He, T. Kraus, N. Li, E. Mena-Osteritz, P. Weitz, T. Heumüller, K. Zhang, C. J. Brabec, P. Bäuerle, *Adv. Mater.* **2022**, *34*, 2103573.

35. S. Zhou, D. Xia, S. Liang, B. Liu, J. Wang, C. Xiao, Z. Tang, W. Li, *ACS Appl. Mater. Interfaces* **2022**, *14*, 7093.

36. C. Kim, J. Liu, J. Lin, A. B. Tamayo, B. Walker, G. Wu, T. -Q. Nguyen, *Chem. Mater.* **2012**, *24*, 1699.

37. G. Feng, J. Li, F. J. M. Colberts, M. Li, J. Zhang, F. Yang, Y. Jin, F. Zhang, R. A. J. Janssen, C. Li, W. Li, *J. Am. Chem. Soc.* **2017**, *139*, 18647.

38. G. Feng, J. Li, Y. He, W. Zheng, J. Wang, C. Li, Z. Tang, A. Osvet, N. Li, C. J. Brabec, Y. Yi, H. Yan, W. Li, *Joule* **2019**, *3*, 1765.

39. N. J. Hestand, F. C. Spano, *Chem. Rev.* **2018**, *118*, 7069.

40. A. Sarbu, L. Biniek, J. -M. Guenet, P. J. Mésini, M. Brinkmann, *J. Mater. Chem. C* **2015**, *3*, 1235.

41. S. Ghosh, X. -Q. Li, V. Stepanenko, F. Würthner, *Chem. Eur. J.* **2008**, *14*, 11343.

42. N. J. Hestand, F. C. Spano, *Acc. Chem. Res.* **2017**, *50*, 341.

43. A. E. Clark, C. Qin, A. D. Q. Li, *J. Am. Chem. Soc.* **2007**, *129*, 7586.

44. D. Veldman, S. M. A. Chopin, S. C. J. Meskers, M. M. Groeneveld, R. M. Williams, R. A. J. Janssen, *J. Phys. Chem. A* **2008**, *112*, 5846.

45. K. S. Lee, P. Kim, J. Lee, C. Choi, Y. Seo, S. Y. Park, K. Kim, C. Park, K. Cho, H. C. Moon, *Macromolecules* **2019**, *52*, 6734.

46. J. A. Lim, F. Liu, S. Ferdous, M. Muthukumar, A. L. Briseno, *Mater. Today* **2010**, *13*, 14.

47. P. Miskiewicz, M. Mas-Torrent, J. Jung, S. Kotarba, I. Glowacki, E. Gomar-Nadal, D. B. Amabilino, J. Veciana, B. Krause, D. Carbone, C. Rovira, J. Ulanski, *Chem. Mater.* **2006**, *18*, 4724.

48. L. J. A. Koster, V. D. Mihailetchi, P. W. M. Blom, *Appl. Phys. Lett.* **2006**, *88*, 052104.

49. P. P. Khlyabich, B. Burkhart, B. C. Thompson, *J. Am. Chem. Soc.* **2012**, *134*, 9074.

50. A. K. K. Kyaw, D. H. Wang, V. Gupta, W. L. Leong, L. Ke, G. C. Bazan, A. J. Heeger, *ACS Nano* **2013**, *7*, 4569.

51. S. Karuthedath, A. Melianas, Z. Kan, V. Pranculis, M. Wohlfahrt, J. I. Khan, J. Gorenflot, Y. Xia, O. Inganäs, V. Gulbinas, M. Kemerink, F. Laquai, *J. Mater. Chem. A* **2018**, *6*, 7428.

52. I. A. Howard, R. Mauer, M. Meister, F. Laquai, *J. Am. Chem. Soc.* **2010**, *132*, 14866.

53. S. Karuthedath, Y. Firdaus, R.-Z. Liang, J. Gorenflot, P. M. Beaujuge, T. D. Anthopoulos, F. Laquai, *Adv. Energy Mater.* **2019**, *9*, 1901443.

SUPPORTING INFORMATION

Additional supporting information can be found online in the Supporting Information section at the end of this article.